FLUID DYNAMICS

Dynamics of active liquid interfaces

Raymond Adkins[1]†, Itamar Kolvin[1]*†, Zhihong You[1]†, Sven Witthaus[1],
M. Cristina Marchetti[1,2]*, Zvonimir Dogic[1,2]*

Controlling interfaces of phase-separating fluid mixtures is key to the creation of diverse functional soft materials. Traditionally, this is accomplished with surface-modifying chemical agents. Using experiment and theory, we studied how mechanical activity shapes soft interfaces that separate an active and a passive fluid. Chaotic flows in the active fluid give rise to giant interfacial fluctuations and noninertial propagating active waves. At high activities, stresses disrupt interface continuity and drive droplet generation, producing an emulsion-like active state composed of finite-sized droplets. When in contact with a solid boundary, active interfaces exhibit nonequilibrium wetting transitions, in which the fluid climbs the wall against gravity. These results demonstrate the promise of mechanically driven interfaces for creating a new class of soft active matter.
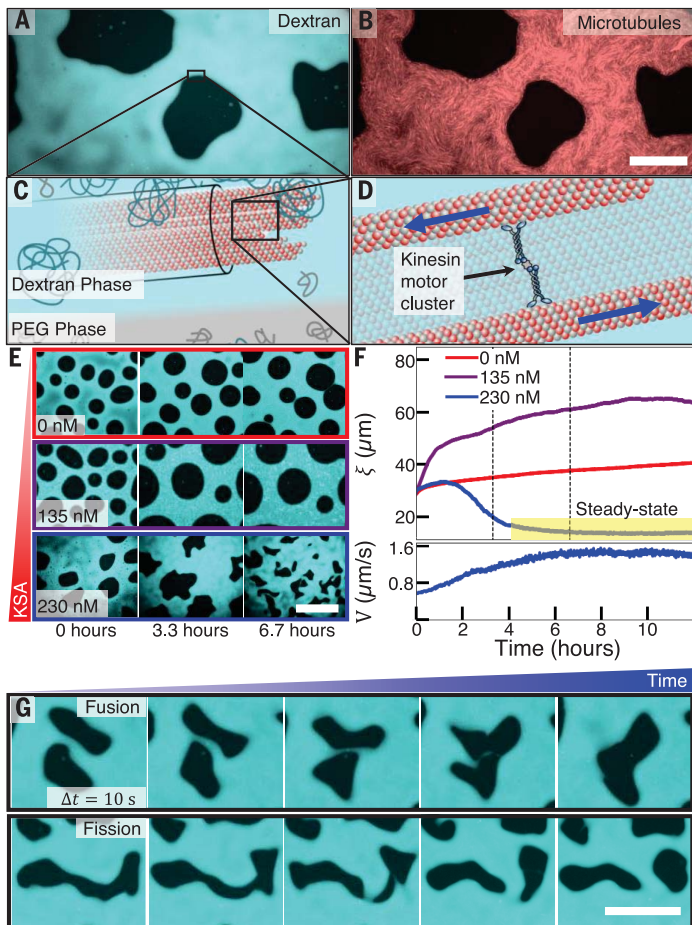
L iquid-liquid phase separation (LLPS) is a ubiquitous phase transition, with examples abounding throughout material science, biology, and everyday life (1, 2). Immiscible liquid phases are separated by sharp but deformable interfaces that strongly couple to flows and the input of mechanical energy. For example, gentle shaking of an oil-water mixture induces gravity-capillary interfacial waves, whereas more vigorous perturbations break up the entire interface, reinitializing the phase separation (3–6). Active matter provides an alternative method of continuously stirring a fluid (7, 8). In such systems, mechanical energy, inputted locally through the motion of microscopic constituents, cascades upward to generate large-scale turbulent-like dynamics (9–11). We studied how active stresses and associated flows perturb soft interfaces and LLPS. Using experiment and theory, we identified universal features of active-LLPS, including giant interfacial fluctuations, traveling interfacial waves, activity-arrested phase separation, and activity-induced wetting transitions. These results demonstrate how active matter drives liquid interfaces to configurations that are not accessible in equilibrium. In turn, active interfaces are elastic probes that provide insight into the forces that drive active fluids—for example, by allowing for the measurement of the active stresses.

The active liquid interfaces we studied belong to a wider class of activity-driven boundaries that includes lipid bilayers, colloidal chiral fluids, and interfaces between motile and immotile bacteria in a swarm (12–16). From a biology perspective, LLPS has emerged as a ubiquitous organizational principle (2, 17).

How cytoskeletal active stresses couple to self-organization of membraneless organelles remains an open question. Studies of simplified systems can shed light on these phenomena. Relatedly, active wetting plays a potential role in the development and shaping of tissues (18).

To explore how activity modifies soft interfaces, we combined poly(ethylene glycol) (PEG) and polysaccharide dextran with stabilized microtubule filaments and clusters of kinesin molecular motors. Above a critical polymer concentration, the passive PEG-dextran mixture phase separated (19). Microtubules and kinesin clusters exclusively partitioned into the dextran phase, in which depletion forces promoted microtubule bundling (Fig. 1, A to C). Streptavidin-bound kinesin clusters (KSA) stepped along adjacent microtubules within a bundle, driving interfilament sliding. The kinesin-powered bundle extensions continuously reconfigured the filamentous network, generating large-scale turbulent-like flows, similar to those previously studied (Fig. 1D) (9). The PEG-dextran interfaces were susceptible to large deformations by active stresses generated within the dextran phase because of their ultralow interfacial tension (<1 µN/m) (19).
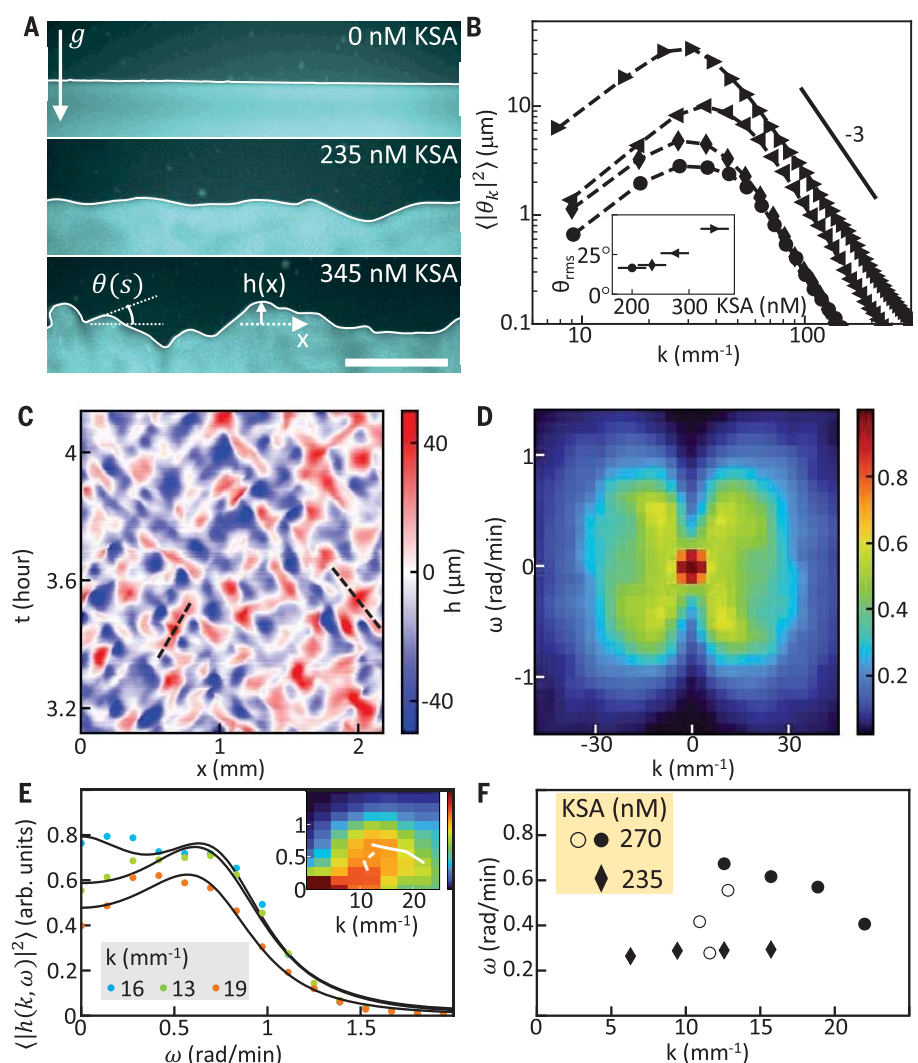
We first visualized the phase separation dynamics of active LLPS in ~30-µm-thick horizontal microscopy chambers. In such samples, PEG-dextran interfaces had a nearly flat vertical

[1]Department of Physics, University of California at Santa Barbara, Santa Barbara, CA 93106, USA. [2]Graduate program in Biomolecular Science and Engineering, University of California at Santa Barbara, Santa Barbara, CA 93106, USA.
*Corresponding author. Email: zdogic@physics.ucsb.edu (Z.D.); cmarchetti@ucsb.edu (M.C.M.); itamar@ucsb.edu (I.K.)
†These authors contributed equally to this work.

Fig. 1. Active LLPS.
(**A**) Coexisting PEG-rich (dark) and dextran-rich (cyan) domains. (**B**) Labeled microtubules (red) are dissolved in the dextran phase. Scale bar, 75 µm. (**C**) Microscopic-scale depiction of phase separation. Minority PEG polymers (gray) in the dextran-rich phase induce microtubule bundling. (**D**) Kinesin clusters drive interfilament sliding. (**E**) Time evolution of the active LLPS at three KSA concentrations. Scale bar, 350 µm. (**F**) (Top) Correlation length evolution ξ(t) for three KSA concentrations. For 230 nM KSA, ξ plateaus at long time (yellow highlight). (Bottom) Root mean square velocity of turbulent flows in the dextran phase at 230 nM KSA. (**G**) Fusion and fission of PEG droplets. Sample chamber thickness, 30 µm. Scale bar, 100 µm.

profile (fig. S1). The quasi–two dimensional (2D) nature of the system was supported by a nearly constant area fraction of the PEG-rich domains (fig. S2). In a passive system with microtubules but no kinesin motors, the droplets coalesced slowly (Fig. 1E and movie S1). The addition of motors altered the coarsening kinetics. At intermediate KSA concentrations, active flows powered droplet motility, which increased the probability of droplets encountering each other and coalescing, thus speeding up coarsening dynamics (Fig. 1E and movie S2). Higher KSA concentrations accelerated buildup of interfacial fluctuations, leading to an entirely different dynamical state in which droplets incessantly fused and fissioned with each other (Fig. 1, E and G, and movie S3).

To quantify the influence of activity on the PEG-dextran phase separation, we measured the equal-time two-point correlation function $C(\Delta \mathbf{r}, t) = \langle I(\mathbf{r} + \Delta \mathbf{r}, t) I(\mathbf{r}, t) \rangle_{\mathbf{r}}$, where $I = 1$ in the dextran phase and –1 otherwise (fig. S3). Spatial correlations decayed over a length scale ξ, defined by $C(\xi) = 0.5$, which is comparable with the average droplet size (fig. S4). For passive samples, ξ increased slowly in time (Fig. 1F). Enhanced coarsening at intermediate KSA concentration was reflected by a much faster initial growth of ξ than the passive case. At high motor concentration, ξ peaked at ~1 hour and subsequently decayed to a finite plateau, ξ_{steady}. In parallel, average interface curvature κ monotonically grew, reaching a sufficiently large value to cause droplet fission (fig. S5). The steady-state length scale ξ_{steady} was maintained by the balance of droplet fission and fusion events, in which ξ_{steady} was comparable with the inverse of the average interface curvature κ_{steady}. Concomitantly with the plateauing of ξ, active flow speed became constant (Fig. 1F). These results demonstrate activity-suppressed coarsening dynamics, which created an emulsion-like state in which finite-sized droplets continuously merge, break apart, and exchange their content (Fig. 1G and movies S3 and S4). The volume fractions of the active and passive phases were nearly equal (fig. S2). Low volume fraction of active fluid generated similar steady states. Finite-sized domains are reminiscent of theoretical prediction in motility-induced phase separation of isotropic active particles (20). However, in contrast to theory, the active fluid in our experiments is anisotropic and perturbs an underlying equilibrium phase separation.

To gain insight into how active stresses drive interfacial fluctuations, we formed a macroscopic interface through gravity-induced bulk phase separation (Fig. 2A and fig. S6). In equilibrium, molecular motion works against the density difference $\Delta \rho$ and interfacial tension γ to roughen the liquid-liquid interface. Typical disturbances of PEG-dextran interfaces, bereft

of activity, are ~100 nm in amplitude, resulting in boundaries that appear flat when viewed with our imaging setup (Fig. 2A and fig. S7). When driven out of equilibrium, however, interfaces exhibited giant undulations that were visible with the naked eye (movie S5). As motor concentration increased, interfaces became multivalued with frequent overhangs, indicating that active stresses directly control interface configurations (Fig. 2A and movie S6).

The interplay of activity and capillarity is clarified by measuring the interfacial fluctuation spectrum. To this end, local interface tangent angles $\theta(s, t)$ were sampled at a time t as a function of the arc-length distance s along

Fig. 2. Active propagating waves. (**A**) Conformations of bulk phase–separated interfaces with increasing motor (KSA) concentration. $\theta(s)$ defines the local interface tangent angle as a function of arc length. $h(x)$ is the local interface height. Chamber thickness, 60 μm. Scale bar, 150 μm. (**B**) θ power spectra obtained by averaging over ~3-mm interface length, 6 to 8 hours after sample preparation. (Inset) Root mean square θ versus KSA concentration. (**C**) Space-time map of h. Disturbances propagating along the interface (dashed lines). Interfaces were corrected for drift and tilt. (**D**) The square-root DSF averaged 4 to 6 hours after sample preparation. Maximum lag distance, 1000 μm; maximum lag time 1800 sec. (**E**) DSF sections at constant wave number (colored dots). Black lines are best approximations with

$$F(\omega) = a\left[(\omega/\omega_1)^2 + 1\right]^{-1} + b\left\{\left[(\omega/\omega_0)^2 - 1\right]^2 + (\omega \Delta \omega / \omega_0^2)^2\right\}^{-1}, \text{ where } a, b, \omega_1, \omega_0, \text{ and } \Delta\omega \text{ are}$$

adjustable parameters. Data were taken over 2 to 4 hours after sample preparation. (Inset) Frequency peaks $\omega_p = \sqrt{\omega_0^2 \Delta\omega^2 / 2}$ overlayed on DSF intensity (full line). DSF maxima for constant ω (dashed line). For (C) to (E), KSA concentration, 270 nM. (**F**) Peak frequencies of the propagating modes ω_p (solid symbols). DSF maxima at constant frequency sections (open symbols).

Fig. 3. Numerical hydrodynamics of active interfaces. (A) Phase boundary (cyan) separating a passive fluid (black) and an active isotropic liquid crystal. The latter are depicted with local order parameter (grayscale) and orientation (red lines). Legends denote activities $|\alpha|$. Scale bar, 100 μm. **(B)** θ power spectra. Simulation interval, 2 mm. Correlation maximum lag distance, 400 μm. (Inset) Root mean square θ versus $|\alpha|$. **(C)** Square root DSF. $|\alpha| = 40$ mPa. Maximum lag time, 270 s. Maximum lag distance, 670 μm. Total simulation time, 3 hours. Simulation interval, 2 mm. **(D)** Constant wave number sections of DSF intensity (solid circles). Best approximations $F(\omega)$ are as in Fig. 2E (black lines). $|\alpha| = 20$ mPa. (Inset) $\omega_p(k)$ overlay on DSF intensity (solid line) and DSF maxima for constant ω (dashed line). **(E)** Peak frequencies of the propagating modes ω_p (solid symbols) and DSF maxima for constant ω (open symbols). Activities are noted in absolute values.
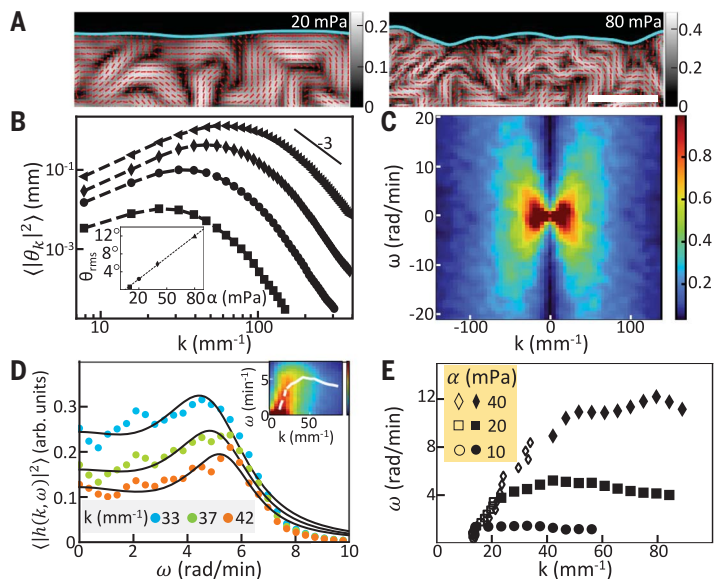
Fig. 4. Active wetting transition. (A) Active fluid wetting a polyacrylamide-coated vertical boundary at three KSA concentrations. Scale bar, 50 μm. **(B)** Magnified section of the wetting layer at 345 nM KSA showing local orientations of microtubule bundles. Scale bar, 20 μm. **(C)** Average center-of-mass height of active fluid within $5\ell_e$ of the vertical boundary, where $\ell_e = 45$ μm. Zero height is defined as the average bulk interface position. Each point is the mean of two experiments. Uncertainty in sample preparation is indicated with horizontal bars. (Inset) Average wetting height profiles as a function of distance from the vertical boundary. KSA concentrations, 180 nM (blue) to 270 nM (red). Black line indicates $\sim e^{-x/\ell_e}$. **(D)** Wetting profiles from numerical simulations. Equilibrium contact angle is $\theta_e = 10°$. Interface position is in cyan. Scale bar, 50 μm. (Inset) Local liquid crystalline orientation (red lines). **(E)** Center-of-mass height of the numerical wetting profile. Red line indicates prediction of Eq. 3 with $\ell_w = 2.5$ μm. Onset of complete wetting is indicated with the blue arrow. (Inset) Average numerical wetting profiles. Activities are 10 mPa (blue) to 40 mPa (red).
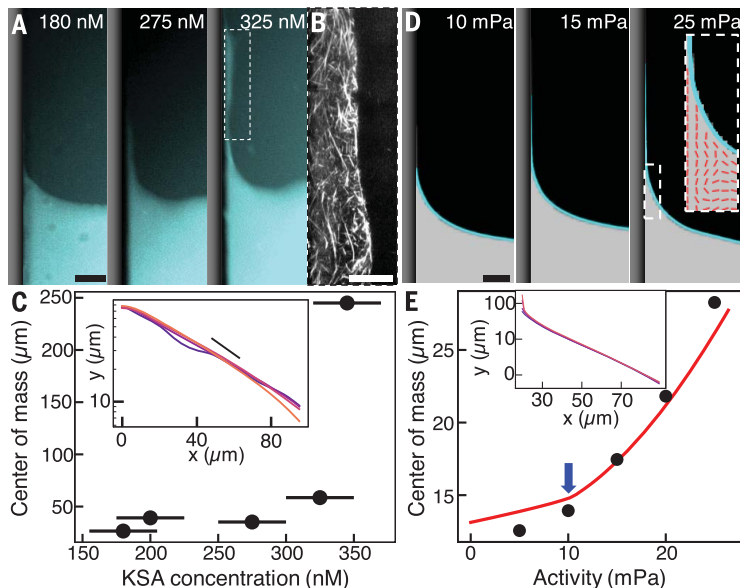
the interface (Fig. 2A). Interfacial fluctuations were described by time-averaged power spectra $S(k) = \langle\|\theta_k\|^2\rangle_t$, with $\theta_k = \int ds\,\theta(s,t)e^{-iks}$. Because of equipartition of thermal energy among Fourier modes, the spectrum of equilibrium interfaces is $S(k) \sim Tk^2/(k^2 + k_c^2)$, where T denotes temperature. The capillary wave number $k_c = \sqrt{\Delta\rho g/\gamma}$ sets a crossover from a gravity-dominated regime at large scales $S(k) \sim k^2$ to a plateau at small scales, where surface tension attenuates fluctuations. Active interfacial fluctuations were markedly different. Active spectra $S(k)$ increased for small wave numbers (Fig. 2B and figs. S7 and S8). After reaching a maximum for $k_m \sim 30$ mm^{-1}, it decayed as $S(k) \sim k^{-3}$, instead of plateauing

as in equilibrium. Whereas the shape of $S(k)$ remained the same for all KSA concentrations, the root mean square tangent angle θ_{rms} increased linearly with activity (Fig. 2B, inset). Using the crossover at k_m as a determinant of the fluctuation amplitude, it would take an effective temperature of ~$10^{11}K$ to achieve equilibrium interfaces whose roughness is comparable with those measured at the lowest activities.

The dynamics of activity-driven interfacial fluctuations exhibited nontrivial spatiotemporal correlations. To gather sufficient statistics, we imaged ~10-mm-long active interfaces over a 2-hour interval. Space-time maps of local interface height $h(x, t)$ exhibited diagonally streaked crests and troughs that were sug-

gestive of propagating waves (Fig. 2C). These translational modes were also evident in time-lapse movies (movie S6). To characterize these modes, we measured the dynamic structure factor (DSF) of the interface height $D(k, \omega) = \int dx\,dt\,e^{ikx+i\omega t}\langle h(x',t')h(x'+x,t'+t)\rangle_{x',t'}$ (Fig. 2D). Over a finite range of wave numbers, the DSF exhibited peaks at finite frequencies ω_p, confirming the presence of propagating modes (Fig. 2E). Increased KSA concentration resulted in higher ω_p for the same wave numbers; thus, activity controlled the phase velocity (Fig. 2F).

The giant nonequilibrium fluctuations and propagating wave modes result from the interaction of active flows in the bulk dextran phase with interfacial elasticity. To elucidate the processes that drive active interfaces, we

numerically integrated 2D hydrodynamic equations that describe a bulk phase–separated active fluid (21, 22). The two coexisting phases were modeled as incompressible Newtonian fluids under gravity that experience confinement friction in the low Reynolds number limit (23). The top phase was passive, whereas the velocity of the bottom phase **v** was governed by
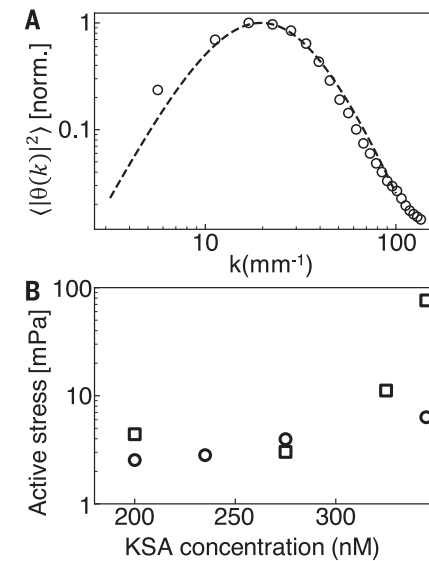
$$\gamma_v \mathbf{v} - \eta \nabla^2 \mathbf{v} = -\nabla P + \nabla \cdot \boldsymbol{\sigma} \qquad (1)$$

where P is the pressure, η is the viscosity, and γ_v is the confinement friction. The stresses $\boldsymbol{\sigma}$ driving the flows were assumed to be generated by an active liquid crystal producing extensile active stresses, $\boldsymbol{\sigma}^a = \alpha \mathbf{Q}$, with $\alpha < 0$. The local orientational order was quantified by a traceless tensor $Q_{ij} = \langle \hat{n}_i \hat{n}_j - \delta_{ij}/2 \rangle$ averaged over molecular orientations $\hat{\mathbf{n}}$. Active shear flows engendered orientational order through flow-induced alignment. These assumptions are summarized in the continuum equation

$$\frac{D\mathbf{Q}}{Dt} + [\boldsymbol{\omega}, \mathbf{Q}] = \lambda \mathbf{u} + \frac{1}{\lambda_Q} \mathbf{H} \qquad (2)$$

where $\boldsymbol{\omega}$ is the vorticity tensor, $\mathbf{u}$ is the strain rate, and λ is the flow alignment parameter. $\mathbf{H}$ denotes elastic forces that arise from the liquid crystal free energy, and γ_Q is the rotational viscosity of microtubule bundles (23). In the absence of activity, the liquid crystal is in the isotropic phase, which is consistent with the microtubule density used in experiments.

The hydrodynamic model reproduces key experimental observations. Finite-sized chaotic flows, driven by active stresses, continuously deform the liquid-liquid interface (Fig. 3A and movie S7). Similarly to experiments, the interfacial power spectra showed a crossover between growth at small wave numbers and decay at large wave numbers, whereas the root mean square tangent angle increased linearly with $|\alpha|$ (Fig. 3B). The numerically obtained DSF also exhibited signatures of active traveling waves (Fig. 3, C to E), as in the experiment. The wave frequencies $\omega_p(k)$ increased with activity, showing active-stress–dependent wave velocity. Our numerical model also suggests a noninertial mechanism of active waves (12), which differs from conventional inertia-dominated capillary waves (24, 25). In the context of our hydrodynamic model, the active waves arise from the coupling between the interface vertical displacement h and orientational order Q in the interfacial region (22). Stress balance at the interface predicts that the orientational order drives interfacial deformation as $\partial_t h \sim v_\perp^a \sim \alpha |k| Q$, where $v_\perp^a$ is the active contribution to the flow velocity normal to the interface. In turn, passive flows $v_\perp^p$ relaxing the interface at a wave number dependent rate $\nu(k)$ feed back to induce local liquid crystalline

order $\partial_t Q \sim \lambda i k v_\perp^p \sim -\lambda i k \nu(k) h$. Consequently, interface height obeys a wave equation $\partial_t^2 h \sim -\alpha \lambda i k |k| \nu(k) h$ (23). Accordingly, traveling wave velocities increase with active stress, which is in agreement with both experiments and numerics.

Propagating waves might be a generic feature of active boundaries (12, 13). More broadly, the active-stress–dependent wave dispersion mirrors those of elastic waves in entangled polymers solutions (26). Although the numerical hydrodynamics reproduced qualitative features of the experimentally observed active fluctuations and waves, there were important quantitative differences. In particular, with increasing activity, numerics predicted an increase in both interface fluctuations and bulk velocity. By contrast, in experiments active flows remained constant between 200 and 350 nM KSA, whereas interfacial fluctuations increased (fig. S9). Moreover, in numerics, the maximum wave number k_m increased with activity while remaining constant in experiments (Figs. 2B and 3B and fig. S10).

Fig. 5. Active stress estimation from interface fluctuations and wetting. (**A**) Normalized tangent angle power spectrum. KSA concentration, 200 nM (circles). Analytical hydrodynamic prediction is indicated with the dashed line (eq. S35). (**B**) Root mean square active stress estimates from interfacial fluctuations $\sigma_{rms} = p\theta_{rms}$ (circles). Experimental θ_{rms} are as in Fig. 2B, inset. Analytical hydrodynamic theory (Eq. 1 and eq. S35) predicts p = 8.8 mPa/rad, by using active length scale ℓ_a = 65 µm and time scale τ_a = 77 s that were derived from bulk flow correlations (fig. S13). Active stress estimates from wetting $\sigma^a = 4(h_{cm} - h_{cm}^0)\Delta\rho g$ (squares). h_{cm} is the wetting center-of-mass height (Fig. 4C). h_{cm}^0 equals h_{cm} for 180 nM KSA.

To demonstrate the particular properties of active interfaces, we studied their structure next to a solid boundary (Fig. 4, A and B). In the absence of motors, the interface assumed an exponential profile $h \propto e^{-x/\ell_e}$ with a decay length of $\ell_e \sim 45$ µm, which we identified with the capillary length $\ell_c = \sqrt{\gamma/\Delta\rho g}$. At the wall, the rise in the interface height was ~70 µm, which is close to the maximum capillary rise of $\sqrt{2}\ell_c$, indicating complete wetting (23). At intermediate KSA concentrations, the capillary rise exhibited active fluctuations around the equilibrium exponential height profile, and the time-averaged center-of-mass height of the wetting region increased slowly (Fig. 4C). Above a critical value of 300 nM KSA, activity generated a new interfacial structure. Specifically, we observed formation of a ~20-µm-thick dynamical wetting layer, which climbed several hundred micrometers above the equilibrium capillary rise (Fig. 4A and movie S8). Within this layer, microtubule bundles preferentially aligned with the wall (Fig. 4B). Coinciding with the appearance of the microtubule-rich wetting layer, the mean capillary rise sharply increased (Fig. 4C). These observations demonstrate an activity-driven wetting transition beyond the complete wetting of a passive fluid.

We performed numerical simulations of the active-interface adjacent to a vertical boundary (23). The liquid crystal director was anchored parallel to the wall, and the surface-liquid energy γ_w corresponded to an equilibrium contact angle 10° (Fig. 4D). Similar to experiments, the average height profile had an exponential decay (Fig. 4E, inset). As the activity α increased from zero, the height of the contact point increased. Furthermore, above $|\alpha| = 10$ mPa, the active fluid generated a thin wall-adjacent layer, indicating a transition from partial to complete wetting (Fig. 4D and movie S9). The capillary rise was supported by a ~3-µm-thick ℓ_w, vertically aligned liquid crystalline domain, with $Q \sim 1$. This domain generated coherent active stress along the wall $\sigma^a = \alpha$, which supported the interface rise. Balancing the active tension $\gamma_a \equiv |\sigma^a|\ell_w$ at the contact point with wall adhesion γ_w, surface tension $\gamma\cos\theta_a$, and gravity F_g resulted in a boundary condition for the climbing interface (fig. S11) (23).

$$|\sigma^a|\ell_w + \gamma_w = \gamma\cos\theta_a + F_g \qquad (3)$$

Predictions of the center-of-mass height of the capillary rise, using Eq. 3, show a crossover from slow to fast growth at α = 10 mPa, which is in agreement with the partial-to-complete wetting transition seen in simulations (Fig. 4E and fig. S12).

Active interfaces provide a distinct experimental probe with which to estimate the magnitude of the active stress, a critical parameter that governs dynamics of active fluids. To avoid resorting to various assumptions

on the numerical model, we analytically solved Eq. 1, treating the stress σ as a random field with correlations $\langle \sigma_{ij}(\mathbf{r},t)\sigma_{ij}(\mathbf{0},0)\rangle = \sigma_{\mathrm{rms}}^2 e^{-|\mathbf{r}|/\ell_a - |t|/\tau_a}$, where correlation length ℓ_a and time τ_a are identified with those of the bulk active flow (fig. S13) (23). The analytical model captured the interface fluctuations spectrum $S(k)$ without fitting parameters, revealing that its nonmonotonic shape resulted from active flows with scale-dependent kinetic energy spectrum (Fig. 5A, fig. S10, and eq. S32) (23, 27). By contrast, fluctuations of equilibrium interfaces are driven by thermal energy $\sim k_B T$, where k_B is the Boltzmann constant, that is equally distributed among all scales (23). By integrating $S(k)$ over all wave numbers, the active stress is predicted to increase proportionally to tangent angle fluctuations $\sigma_{\mathrm{rms}} = p\theta_{\mathrm{rms}}$, with $p \simeq 9$ mPa/rad (Fig. 5B and eq. S35).

To independently verify these numbers, the force balance Eq. 3, which is associated with active wetting, provides an alternative method of estimating active stress. For intermediate KSA values, before the appearance of the active wetting layer, the active stress estimated from wetting is comparable with those extracted from interface fluctuations (Fig. 5B). Above 300 nM KSA, active stresses are a few times larger than those obtained from interface fluctuations. These large values might be a consequence of flow-enhanced alignment of microtubule bundles within the thin wetting layer. The formation of the active wetting layer at finite activity, however, is outside the scope of the static stress balance embodied in Eq. 3. A more complete description of the wetting transition would include dynamical considerations, such as active wave propagation and gravitational sedimentation, that appear to be essential for the formation and turnover of the wetting layer.

We demonstrated a rich interplay between active fluids and soft deformable interfaces.

Liquid interfaces provide a quantitative probe that can reveal intrinsic properties of the active fluids, such as active stress. As well, bulk active fluids drive the extreme interfacial deformations that yield intriguing nonequilibrium dynamics, including arrested phase separation, stress-dependent noninertial propagating waves, and activity-controlled wetting transitions. Our findings provide a promising experimental platform by which to design shape-changing adaptable soft materials and machines whose capabilities begin to match those observed in biology (28–30).

REFERENCES AND NOTES

1. A. J. Bray, *Adv. Phys.* **51**, 481–587 (2002).
2. C. P. Brangwynne et al., *Science* **324**, 1729–1732 (2009).
3. J. O. Hinze, *AIChE J.* **1**, 289–295 (1955).
4. P. Tong, W. I. Goldburg, J. Stavans, A. Onuki, *Phys. Rev. Lett.* **62**, 2668–2671 (1989).
5. L. Berthier, J. L. Barrat, J. Kurchan, *Phys. Rev. Lett.* **86**, 2014–2017 (2001).
6. P. Perlekar, R. Benzi, H. J. H. Clercx, D. R. Nelson, F. Toschi, *Phys. Rev. Lett.* **112**, 014502 (2014).
7. R. Aditi Simha, S. Ramaswamy, *Phys. Rev. Lett.* **89**, 058101 (2002).
8. M. C. Marchetti et al., *Rev. Mod. Phys.* **85**, 1143–1189 (2013).
9. T. Sanchez, D. T. N. Chen, S. J. DeCamp, M. Heymann, Z. Dogic, *Nature* **491**, 431–434 (2012).
10. H. H. Wensink, *Proc. Natl. Acad. Sci. U.S.A.* **109**, 14308–14313 (2012).
11. S. Zhou, A. Sokolov, O. D. Lavrentovich, I. S. Aranson, *Proc. Natl. Acad. Sci. U.S.A.* **111**, 1265–1270 (2014).
12. H. Soni, W. Luo, R. A. Pelcovits, T. R. Powers, *Soft Matter* **15**, 6318–6330 (2019).
13. V. Soni et al., *Nat. Phys.* **15**, 1188–1194 (2019).
14. A. E. Patteson, A. Gopinath, P. E. Arratia, *Nat. Commun.* **9**, 5373 (2018).
15. S. C. Takatori, A. Sahu, *Phys. Rev. Lett.* **124**, 158102 (2020).
16. H. R. Vutukuri et al., *Nature* **586**, 52–56 (2020).
17. C. M. Caragine, S. C. Haley, A. Zidovska, *eLife* **8**, e47533 (2019).
18. C. Pérez-González et al., *Nat. Phys.* **15**, 79–88 (2019).
19. Y. Liu, R. Lipowsky, R. Dimova, *Langmuir* **28**, 3831–3839 (2012).
20. R. Singh, M. E. Cates, *Phys. Rev. Lett.* **123**, 148005 (2019).
21. L. Giomi, A. DeSimone, *Phys. Rev. Lett.* **112**, 147802 (2014).
22. L. Matthew, *Phys. Rev. Lett.* **113**, 1–5 (2014).
23. Materials and methods are available as supplemental materials.
24. D. Langevin, *Light Scattering by Liquid Surfaces and Complementary Techniques* (CRC Press, 1992).
25. D. G. A. L. Aarts, M. Schmidt, H. N. W. Lekkerkerker, *Science* **304**, 847–850 (2004).
26. A. Varshney, V. Steinberg, *Nat. Commun.* **10**, 652 (2019).
27. B. Martínez-Prat et al., *Phys. Rev. X* **11**, 031065 (2021).
28. J.-F. Joanny, S. Ramaswamy, *J. Fluid Mech.* **705**, 46–57 (2012).
29. E. Tjhung, A. Tiribocchi, D. Marenduzzo, M. E. Cates, *Nat. Commun.* **6**, 5420 (2015).
30. Y. -N Young, M. J Shelley, D. B Stein, *Math. Biosci. Eng.* **18**, 2849–2881 (2021).
31. R. Adkins, I. Kolvin, Z. You, S. Witthaus, M. C. Marchetti, Z. Dogic, Dynamics of active liquid interfaces. Dryad (2022); https://doi.org/10.25349/D9JS6Q.

SUPPLEMENTARY MATERIALS

science.org/doi/10.1126/science.abo5423
Materials and Methods
Figs. S1 to S13
References (32–57)
Movies S1 to S9

Science

Dynamics of active liquid interfaces

Raymond AdkinsItamar KolvinZhihong YouSven WitthausM. Cristina MarchettiZvonimir Dogic

When active and passive fluids interact

Incompatible liquids such as oil and water will phase separate with low interfacial tension. Adkins *et al.* investigated the dynamics of a one-dimensional interface separating an active nematic phase with a passive isotropic phase (see the Perspective by Palacci). They found a rich behavior of fluctuating interfaces in which the phase-separating fluids could form active emulsions that did not coarsen and in which droplets formed spontaneously. Macroscopic interfaces can also displayed propagating waves with a characteristic wave number and speed. Furthermore, the activity of one of the fluids, in which the addition of energy drove the ordering of that fluid, was able to modify the wetting transitions. The authors also observed active wetting of a solid surface whereby active extensile stresses parallel to the surface drove the fluid to climb a solid wall against gravity. —MSL

View the article online
https://www.science.org/doi/10.1126/science.abo5423
Permissions
https://www.science.org/help/reprints-and-permissions

Use of this article is subject to the Terms of service